Clean Energy Science and Technology 2024, 2(3), 201
https://doi.org/10.18686/cest.v2i3.201

Article

Optimization of fish-friendly bulb turbine based on orthogonal method and computational fluid dynamics

Xiuli Mao[1,2,3,*], Jiahao Lu[4], Chuang Cheng[4], Zhenggui Li[2], Diyi Chen[1,4], Wei Han[5], Jiaren Hu[1,4], Tianyu Cao[1,4]

[1] Key Laboratory of Agricultural Soil and Water Engineering in Arid and Semiarid Areas, Ministry of Education, Northwest A&F University, Yangling 712100, China
[2] Key Laboratory of Fluid and Power Machinery (Xihua University), Ministry of Education, Chengdu 610039, China
[3] School of Fundamental Science and Engineering, Waseda University, Tokyo 169-8555, Japan
[4] College of Water Resources and Architectural Engineering, Northwest A&F University, Yangling 712100, China
[5] College of Energy and Power Engineering, Lanzhou University of Technology, Lanzhou 730050, China
*** Corresponding author:** Xiuli Mao, maoxl@nwafu.edu.cn

CITATION

Mao X, Lu J, Cheng C, et al. Optimization of fish-friendly bulb turbine based on orthogonal method and computational fluid dynamics. Clean Energy Science and Technology. 2024; 2(3): 201. https://doi.org/10.18686/cest.v2i3.201

ARTICLE INFO

Received: 16 July 2024
Accepted: 2 August 2024
Available online: 28 August 2024

Abstract: A high-performance, fish-friendly bulb turbine was developed in this study by optimizing a runner with spiral blades to enhance the flow passage for fish. The key aspect of this work is multi-objective optimization based on the orthogonal method. Four factors were focused on: the number of guide vanes, the wedge angle of the blades, the distance of vaneless space, and the pitch variation ratio. The optimal value of each design parameter was determined through comprehensive measurements, including intuitive analysis, range analysis, and synthetical frequency analysis. The evaluating indexes were unit output, efficiency, fish-passing damage rate, pressure fluctuation, maximum blade deformation, and equivalent stress. The results indicate that the pitch ratio parameter significantly affected hydraulic performance, while the number of guide vanes primarily influenced fish-passing performance. The optimized turbine achieved a hydraulic efficiency of 84.05%, with a fish damage rate of only 0.01%. Structurally, the vibration modes of the runner were mainly oscillating deformation, rotating deformation around the axis, and bending deformation. The difference between the hydraulic excitation frequencies and the natural frequencies of the runner exceeded 20%, ensuring no resonance under the best efficiency point (BEP) condition. The dry and the prestressed modals showed similar natural frequencies and vibration patterns for the runner, whereas the wet modal showed higher natural frequencies for the runner.

Keywords: tidal energy; fish-friendly bulb turbine; multi-objective optimization; hydraulic performance; structural characteristics

1. Introduction

China, located on the west coast of the Pacific Ocean, boasts a vast sea area and a tortuous coastline rich in tidal energy resources. According to the "908 Special Project" investigation, the total tidal energy resources within the 10 m isobath of the Chinese offshore (excluding Taiwan) amount to 1.9286×10^8 kW. Among these, there are 171 tidal power sites with over 500 kW capacity, resulting in a technically developable capacity of 2,2830 MW [1]. Recent technological development and improvements in system design and turbine technology suggest that the total supply of tidal power may be significantly higher than previously estimated, with economic and environmental costs reduced to competitive levels [2,3]. Compared with other forms of ocean energy, tidal energy offers advantages such as high energy density and predictability, making it a viable supplementary method for electricity generation [4,5].

Previously, the development of tidal energy has been constrained by high operation costs and technological limitations, leading to the operation of only a few tidal plants worldwide, most of which are built in bays with large tidal fluxes [6,7]. For example, Canada's Bay of Fundy has the world's largest tidal range at 16.2 m. Tidal energy is converted into potential energy by creating reservoirs, where the tides' rise and fall determine the water level. The potential energy of seawater drives a hydraulic turbine, converting mechanical energy into electricity through a generator rotor [8,9]. However, tidal power generation significantly impacts the ecology, especially the inevitable damage turbines inflict on marine fish [10,11]. Consequently, developing a fish-friendly turbine is a key concern for scholars and is essential for the future development of tidal energy.

Ecological design represents an innovative direction in hydraulic machinery. Increasingly, researchers and turbine manufacturers focus on eco-friendly designs and manufacturing, such as using innovative materials, implementing barriers to alter fish passages, and reducing unit noise. Fish damage mechanisms in turbines mainly include four aspects [12–14], which are mechanical damage from blade impact, pressure damage caused by rapid pressure change, shear damage carried by large shear forces near the solid-liquid boundary, and cavitation damage induced by low pressure, with pressure and shear damages being the most significant. From the aspect of hydraulic performance, this study concentrated on mitigating pressure and shear damages, while mechanical damage and cavitation damage will be investigated in future research.

The structural field is also used to interpret the influence on fish damage, with the number of runner blades and guide vanes being crucial factors [15–17]. Fewer blades and vanes are beneficial to reduce fish damage, especially when turbines operate near design conditions. In addition, smaller clearances at the upper and lower ends of guide vanes reduce shear damage and abrasion damage to fish [18,19]. For runner blades, Archimedes spiral blades effectively eliminate low-pressure vortex, resulting in less pressure damage to fish [20,21]. It is worth mentioning some points of runner blades: (1) fewer runner blades can make more flow through a turbine, while spiral blades provide more work area for flow; (2) a larger pitch of a blade can expand the runner chamber, leading to a longer flow passage for a smaller change of pressure gradient, effectively reducing pressure damage to fish [22]; and (3) continuous flow channels minimize collisions between fish and the ends of runner blades, offering better guidance than traditional runner blades with multiple interval blades [23]. Consequently, a spiral-blade turbine was optimized to achieve a suitable flow passage for fish in this work.

The two other types of public fish-friendly turbines are axial flow turbines and Francis turbines [24,25], which induce additional fish damage due to the 90° turn of the flow streamline from the guide vane to the runner domain. Although a bulb turbine avoids this 90° turn, its intermittent blades still significantly impact fish [26]. Therefore, it is urgent to develop a fish-friendly turbine with a high hydraulic performance for tidal power generation and other low-head hydro-energy applications.

In the study of fish-friendly turbines, the submerged boundary-lattice Boltzmann method has been applied to simulate fish passing through a turbine, providing pressure distribution data on the fish [27]. Experimental research studies showed that fish suffered pressure damage when the environmental absolute pressure was below –15

kPa or the time-varying pressure derivative exceeded –50 kPa/s [28–30]. Furthermore, fish withstood shear damage when the shear strain rate exceeded 500/s [31–33]. These published results form a solid foundation for the present study, and the mentioned thresholds were used as reference values.

A spiral-blade turbine from a previous study was the research object in this work [21]. The orthogonal test method [34,35], along with intuitive and range analyses, were applied to optimize and evaluate design parameters. The three-dimensional flow field and structure field of the turbine were investigated using computational fluid dynamics and fluid-solid coupling methods, which are widely applied in hydraulic machinery research and supported by high-performance computing technologies [34,36–38]. For example, a multi-objective genetic algorithm was employed in a multidisciplinary design of runner blades [39], and the structure optimization of bulb turbines verified the reliability of the orthogonal test method [40].

This study is a continuation of a previous work, which optimized a fish-friendly bulb turbine based on the orthogonal method and carried out numerical simulations in the flow field and structural field to validate an optimal scheme [23]. The present work aimed at developing a high-performance fish-friendly turbine for generating ocean energy and also serving as a concrete case of synergistic development between ecological and hydraulic engineering. New energy generation, such as ocean energy, makes further contributions to the achievement of the "double carbon" goals proposed by China. The structure of this paper is as follows: Section 2 introduces the research object and numerical settings. Section 3 presents the orthogonal scheme design, and Section 4 presents the optimal scheme. Sections 5 and 6 present the results of flow field and structural field analyses, respectively. In the final section, the main study results are summarized.

2. Numerical model and settings

The fish-friendly turbine featured an intake chamber with a bulb, 17 guide vanes with positive curvature, a runner with two spiral blades, and a draft tube (**Figure 1**). The basic parameters are listed in **Table 1**. The 3D flow domain was constructed using SolidWorks, and the mesh of the flow field and structural field was generated using ICEM. Mesh sensitivity was validated in flow field simulations by evaluating efficiency differences. It was found that when the mesh number exceeded 6 million, the efficiency difference was less than 0.1%, and hence the final mesh number adopted for the whole domain was 8.786 million. Monitoring points IP1-IP4, GV1-GV4, R1-R4, and DT1-DT4 were in the bulb, guide vane, runner, and draft tube, respectively.

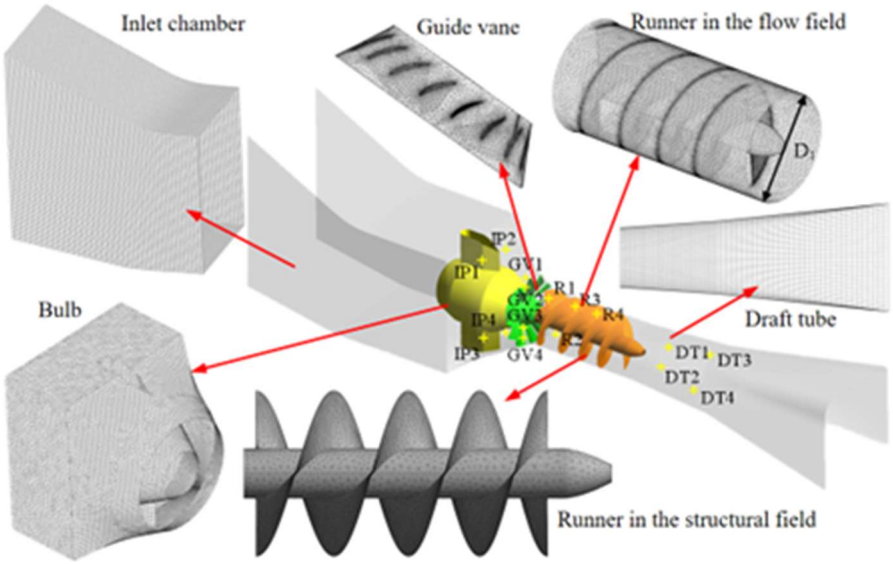

Figure 1. Fish-friendly turbine and its mesh.

Table 1. Basic parameters of fish-friendly turbine.

Parameter	Unit	Value
Design head	m	6.2
Design flow rate	m^3/s	105
Runner diameter	m	5.5
Rated speed	r/min	68
Rated output	MW	5.7
Guide vane number	1	16
Hub ratio	1	0.3
Rated hydraulic efficiency	%	83.43
Pitch variable ratio	1	1.2:0.9

The SST *k*-*ω* model (a turbulence model of shear stress transport) was used to solve the flow field, as it performs well in studying complex flow fields of rotating machinery [23]. The SIMPLEC algorithm was adopted to couple pressure and velocity, with the discrete control equations utilizing a high resolution. Inlet and outlet pressures were determined by the head. A no-slip condition was assumed on the flow walls. The interfaces among different domains were connected using GGI (general grid interface), with the rotor-stator interface set to the "Frozen Rotor" option. The root mean square accuracy of all numerical calculations was 10^{-6}. The time step was Δt = 0.007352941 s, corresponding to 3 degrees of runner rotation. Calculations for all simulations were done using Ansys CFX.

Pressure loads obtained from the flow field were transmitted to the structural field to complete the finite element calculation of runner strength. The modal analysis focused on the rotating part, the material of which was defined as Q345. The density and elastic modulus of Q345 were 7850 kg/m^3 and 212 GPa, respectively, with a yield strength of 345 MPa and a Poisson's ratio of 0.274.

The boundary constraints for the structural field were the gravity and rotation constraints in runner settings. A fixed constraint was imposed on the cylindrical surface at the inlet side of the runner, while other surfaces were defined as interfaces to receive the water pressure (**Figure 2**).

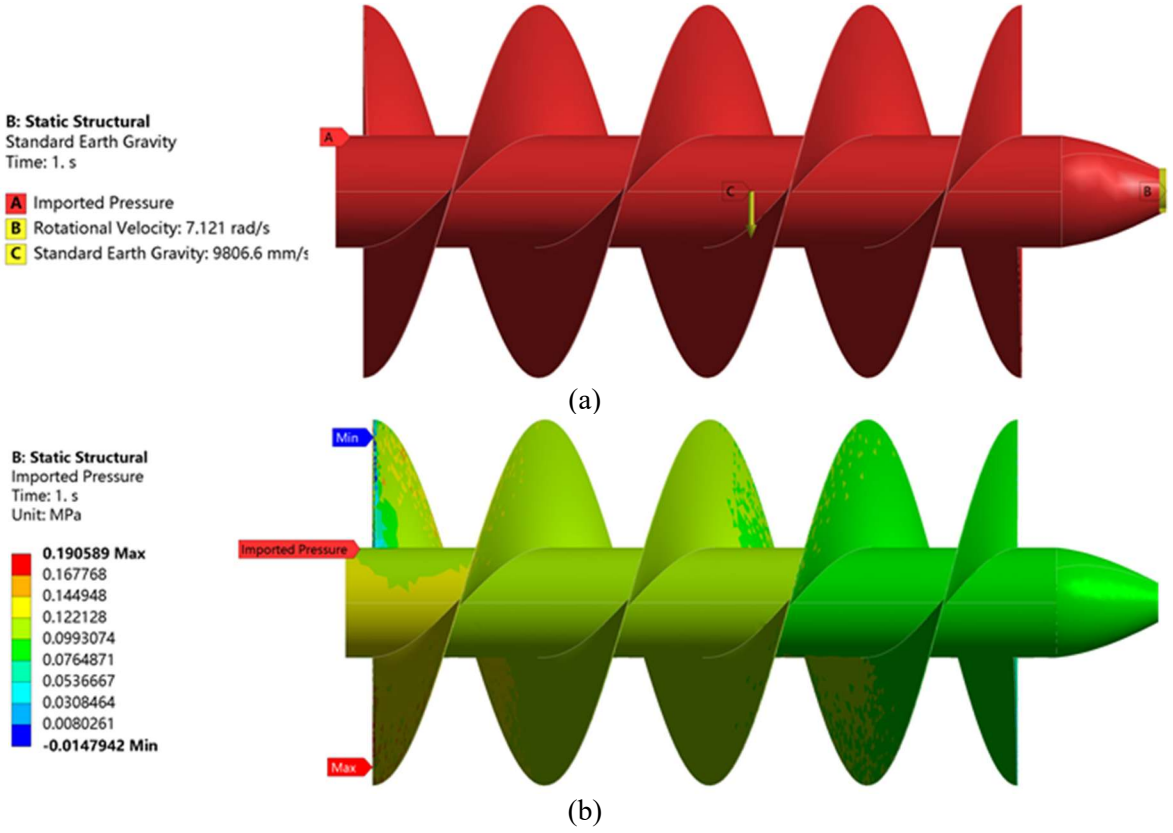

Figure 2. Boundary constraints of structural field: **(a)** solid-boundary constraints and **(b)** water pressures of runner in structural field.

Yellow croaker was taken as the representative fish in this study, as it widely lives in China's eastern coastal areas. Yellow croaker migrates offshore during its breeding period, providing high economic and ecological research values [28]. To simplify the modeling process and save computing resources, the fins of the fish were ignored in the process of model building. As shown in **Figure 3**, the fish model was approximately 27.7 cm in length, with a maximum height and width of 8.3 cm and 5.8 cm, respectively.

Figure 3. Yellow croaker and its 3D model.

3. Orthogonal schemes for optimization

Hydraulic and fish-passing performances were the two optimization objectives for the fish-friendly turbine. Five evaluation indexes were used: output, hydraulic efficiency, pressure fluctuation coefficient, fish-passing damage rate, and maximum blade deformation. The blade diameter ratio, number of blades, blade tip clearance, and distance between the guide vane and blade inlet had been studied in the previous stage [23]. This work focused on four design parameters: the number of guide vanes (G), blade wedge angle (A), distance of vaneless space (D), and pitch ratio (R). The initial values for these parameters were $G = 16$, $A = 1.6°$, $D = 330$ mm, and $R = 1.2{:}0.9$. Based on the orthogonal design method [41], the design parameters in the orthogonal schemes were as follows:

(1) Number of guide vanes

Guide vanes accelerate the incoming flow, forming the required water circulation for the runner. On one hand, more guide vanes are beneficial to flow uniformity and water circulation formation but this also increases fish impact damage. On the other hand, more guide vanes will result in more hydraulic losses and a stronger rotor-stator interaction in a vaneless space. Therefore, configurations with 15, 16, and 17 guide vanes were used, the results of which will be discussed in Section 3. **Figure 4** shows the arrangement of 16 guide vanes, where α is the angle between the guide vane axis and the runner axis ($\alpha = 65°$) and D_T is the throat diameter of the guide vanes ($D_T/D = 0.32$ when $G = 16$).

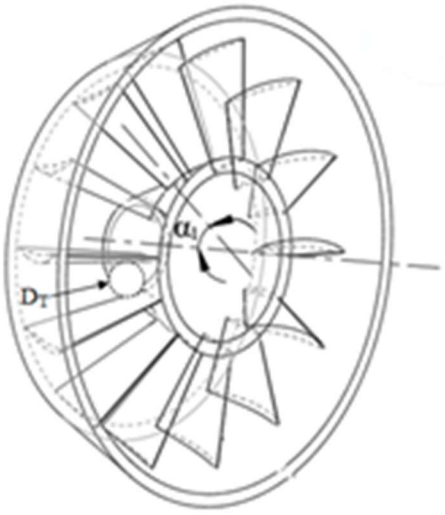

Figure 4. Schematic diagram of 16 guide vanes.

(2) Blade wedge angle

A smaller value of A indicates thinner blades and weaker runner strength, while a higher A increases the excretion coefficient to flow and indicates a larger clearance between the blades and the runner chamber wall, which exacerbates gap cavitation. **Figure 5** is the diagram of A, with values of 1.2°, 1.6°, and 2° investigated, the results of which will be discussed in Section 3.

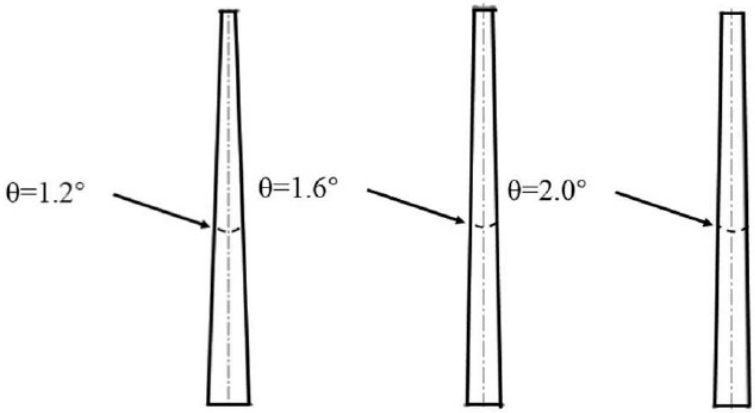

Figure 5. Schematic diagram of blade wedge angle.

(3) Distance of vaneless space

A previous study used the length of a turbine shaft of 8 m with blades occupying 7.2 m and 0.44 m of the vaneless space at the inlet and outlet of the runner, respectively [23]. A longer *D* weakens water circulation formed by the guide vane, which is unfavorable for the energy conversion by the runner. A smaller *D* improves circulation utilization, reduces hydraulic loss, and increases flow circumferential velocity at the guide vane outlet, which enhances the attack angle and aggravates the flow separation degree [42–44]. **Figure 6** shows the various distances of the vaneless space, where 0.33 m, 0.44 m, and 0.55 m were three values of *D* used.

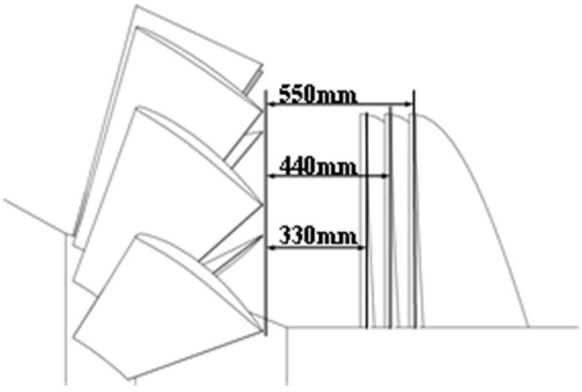

Figure 6. Distances between guide vane and runner blades.

(4) Pitch ratio

The pitch ratio (**Figure 7**) has a decisive influence on the hydraulic efficiency of a turbine. A larger *R* means a longer fish-passing passage and a larger flow surface of blades, while a smaller *R* helps the water flow along the designed streamlines, increasing water utilization efficiency. However, too small an *R* induces increased friction and resistance, decreasing turbine efficiency. The initial pitch was selected as t_r = 0.8D according to models of the Archimedes screw turbine; hence $R = K_{l1}:K_{l2}$ = 1.1:0.9, 1.2:0.9, and 1.2:1.0 were analyzed, where pitch $t = K_l \times t_r$.

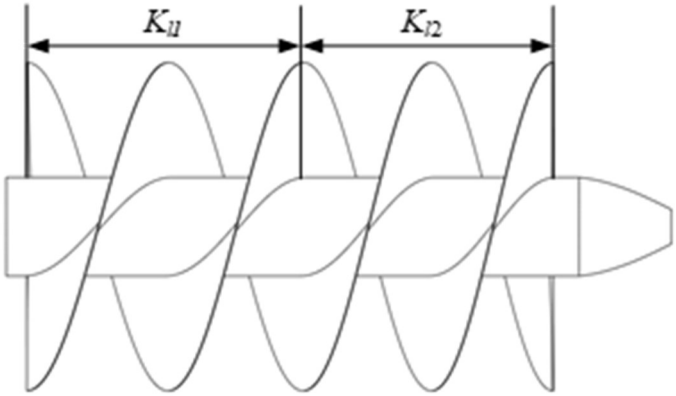

Figure 7. Pitch ratio of blades.

Parameters *G*, *A*, *D*, and *R* mentioned above were considered as the four test factors in the optimization protocols of the orthogonal method, each with three levels. The resulting L9(3^4) orthogonal schemes are shown in **Table 2**.

Table 2. Orthogonal schemes for optimization.

Test scheme	Factor			
	G	***A***	***D***	***R***
1	15	1.2	330	1.1:0.9
2	15	1.6	440	1.2:0.9
3	15	2.0	550	1.2:1.0
4	16	1.2	440	1.2:1.0
5	16	1.6	550	1.1:0.9
6	16	2.0	330	1.2:0.9
7	17	1.2	550	1.2:0.9
8	17	1.6	330	1.2:1.0
9	17	2.0	440	1.1:0.9

4. Selection of optimal schemes

4.1. Intuitive analysis of optimization protocols

The boundary constraints for all simulations in the flow field, which was discussed in Section 2, were identical. The numerical results for each orthogonal scheme are listed in **Table 3**. The output (*N*), hydraulic efficiency (η), fish-passing damage rate ($P(A)$), and pressure fluctuation coefficient (C_p) were calculated using Equations (1) to (4), respectively.

$$N=M\omega \quad (1)$$

$$\eta=M\omega/(9.81QH) \quad (2)$$

$$P(A)=(V_p+V_s)/V_{total} \quad (3)$$

$$C_p=(P-P_a)/P_a \quad (4)$$

where *M*, ω, *Q*, *H*, and *P* represent torque, angular velocity, mass flow, head, and pressure, respectively, while P_a denotes the average pressure, which can be directly obtained from the calculation results. Parameters V_{total} and V_p denote the volume of the

runner chamber and the volume of the space of low-pressure damage, respectively, while V_s represents the volume when the shear force exceeds 500 s^{-1}.

Table 3 lists the calculation results for each scheme. Maximum blade deformation (d_{max}) was derived from structural field analysis.

Table 3. Numerical simulation results.

Test scheme	Evaluating index				
	N **(MW)**	***H*** **(%)**	***P*(*A*)** **(%)**	d_{max} **(mm)**	C_{pmax}
1	5.06	83.02	0.01885050	56.100	0.0017813
2	5.19	85.08	0.01438524	11.353	0.0003684
3	5.09	84.34	0.03704606	24.100	0.0009162
4	5.44	83.76	0.03936444	16.097	0.0003401
5	5.06	83.63	0.05040072	21.812	0.0004025
6	5.21	85.37	0.02907762	15.753	0.0004322
7	5.08	83.50	0.02529560	8.808	0.0007913
8	5.66	84.11	0.01747027	15.156	0.0011302
9	5.04	82.98	0.02507105	18.864	0.0008170

The eighth scheme ($G_3A_2D_1R_3$) exhibited the maximum output at 5.66MW, while the sixth scheme ($G_2A_3D_1R_2$) achieved the best turbine hydraulic efficiency at 85.37%. The lowest fish-passing damage rate was approximately 14.39% in the second scheme ($G_1A_2D_2R_2$), while the 5th scheme showed the maximum fish-passing damage rate of only about 50.4‰, which was significantly lower than that of a traditional bulb turbine [28]. The fourth scheme ($G_2A_2D_1R_3$) demonstrated superior internal fluid stability, indicated by its lower C_{pmax}. In terms of the structural field, the seventh scheme ($G_3A_1D_2R_3$) showed the smallest d_{max} at 0.008808 m. These optimal schemes were identified through intuitive analysis, where the subscript of each factor corresponded to their level, as shown in **Table 2**.

4.2. Range analysis of optimization protocols

The intuitive analysis in Section 4.1 aimed to select the optimal values for each evaluation index by determining the best combinations of different factors and levels, which corresponded to the optimal evaluating indexes. Range analysis was used to estimate the average range of different levels for each factor, where the average range would reflect the influence weight of each factor level on the evaluation index. A larger range would signify a greater influence weight of a factor and its level on the evaluation index. Therefore, this method identified the main factors that significantly affected the evaluating indexes.

The relationship between different factor levels and evaluation indexes was analyzed using range analysis, as shown in **Figure 8**. The *x*-axis represents the design factors with their three levels (corresponding to the subscripts), while the *y*-axis represents $\overline{K_\iota}$. In Equation (5) to Equation (7), K_i is the sum of evaluation index values corresponding to different levels (i) of factors (Y_K), and $\overline{K_\iota}$ is the average value of K_i. With $n = 3$, R_j represents the range.

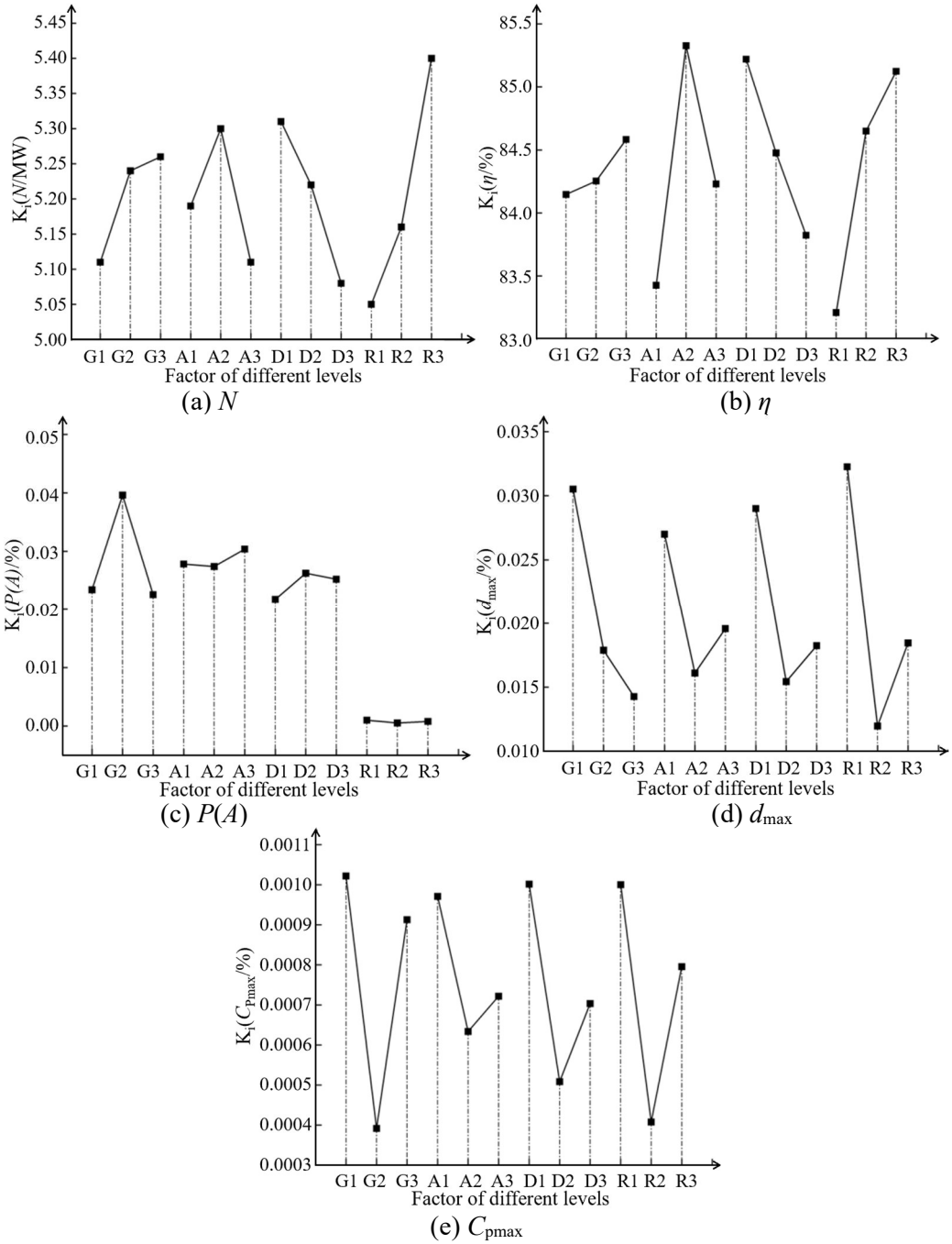

Figure 8. Relationships among different levels of design factors and evaluating indexes.

$$K_i = \sum_{K=1}^{n} Y_k \tag{5}$$

$$\overline{K_i} = \frac{1}{n} K_i \tag{6}$$

$$R_j = max\{\overline{K_1}, \overline{K_2}, \overline{K_3}\} - min\{\overline{K_1}, \overline{K_2}, \overline{K_3}\} \tag{7}$$

The ranges of the evaluation indexes were calculated using Equation (7), the result of which is listed in **Table 4**. Parameter *G* had a significant impact on the evaluation indicators except for output, while the small range of *A* values demonstrated that it is not sensitive to all factors other than η. Parameter *D* had the smallest range of η, whereas its range for other evaluation indicators was not an extreme value. Parameter *R* had higher range values except for *P*(*A*); in other words, *R* greatly

influenced the turbine's hydraulic performance. **Figure 8** illustrates the average impact of different levels of design factors on the evaluation indicators, explained in detail as follows:

Table 4. Ranges of different evaluation indexes.

Range	Evaluating index				
	N (MW)	H (%)	$P(A)$ (%)	d_{max} (mm)	C_{pmax}
$R_j(G)$	0.15	0.72	0.017002	16.242	0.016242
$R_j(A)$	0.19	0.85	0.002979	10.895	0.010895
$R_j(D)$	0.23	0.34	0.004474	13.565	0.013565
$R_j(R)$	0.34	0.86	0.000469	20.287	0.020287

(1) Guide vane number (G): $\overline{K}_i(N)$ and $\overline{K}_i(\eta)$ increased with more guide vanes, peaking when G = 17, while $\overline{K}_i(P(A))$ initially increased and then decreased, with more guide vanes, whereas $\overline{K}_i(d_{max})$ showed a downward trend. Overall, more guide vanes were useful to improve the output and hydraulic efficiency of the turbine, as well as internal fluid stability.

(2) Blade wedge angle (A): $\overline{K}_i(N)$ and $\overline{K}_i(\eta)$ initially increased and then decreased with larger A, peaking at A = 1.6°. On the contrary, $\overline{K}_i(P(A))$, $\overline{K}_i(d_{max})$, and $\overline{K}_i(C_{pmax})$ increased after a decline, reaching their lowest points at A = 1.6° as well. As a consequence, A = 1.6° was the optimal angle for energy conversion and fish-passing of the turbine.

(3) Vaneless distance (D): $\overline{K}_i(N)$ and $\overline{K}_i(\eta)$ showed a downward trend with increasing D, while $\overline{K}_i(d_{max})$ and $\overline{K}_i(C_{pmax})$ had similar characteristics, which were first descending and then ascending with increasing D. On the other hand, $\overline{K}_i(P(A))$ reached its highest point and $\overline{K}_i(C_{pmax})$ was the smallest when D = 440 mm, and hence this value was selected in the optimal scheme.

(4) Pitch ratio (R): $\overline{K}_i(N)$ and $\overline{K}_i(\eta)$ increased monotonically with the continuous increase in R, while $\overline{K}_i(d_{max})$ and $\overline{K}_i(C_{pmax})$ displayed similar changes, falling to their lowest at R = 1.2:0.9. The basically unchanged $\overline{K}_i(P(A))$ indicated that the impact of R on $\overline{K}_i(P(A))$ was negligible. Consequently, the pitch ratio was optimally set at R = 1.2:1.0.

The recommended combinations are given in **Table 5**, based on the result of the range analysis, with the detailed levels of each factor listed as subscripts. The orders of influence of the four factors (R, D, A, and G) on the evaluating indexes were as follows: 1) output: $R > D > A > G$, 2) hydraulic efficiency: $R > A > G > D$, 3) fish-passing damage rate: $G > R > D > A$, 4) blade deformation: $R > G > D > A$, and 5) pressure fluctuation coefficient: $G > R > D > A$.

Table 5. Range analysis of optimal solution.

Evaluating index	N	η	$P(A)$	d_{max}	C_{pmax}
Recommendation	$G_3A_2D_1R_3$	$G_2A_2D_2R_2$	$G_3A_2D_2R_2$	$G_3A_2D_2R_2$	$G_2A_2D_2R_2$

The purpose of synthetical frequency analysis was to determine the influence frequency of different factors (R, D, A, and G) on the evaluating indexes (N, η, $P(A)$, d_{max}, and C_{pmax}). According to the research results in Section 4.2, five optimal schemes were obtained through intuitive analysis and range analysis, respectively. When the five recommended schemes from intuitive analysis ($G_3A_2D_1R_3$, $G_2A_3D_1R_2$, $G_1A_2D_2R_2$, $G_2A_2D_1R_3$, and $G_3A_1D_2R_3$ in Section 4.1) were combined, the number of scenarios of 10 was used as the denominator, as shown in **Table 6**, while the numerator represents the number of occurrences of each factor level in the ten scenarios. Parameter values G_3 = 17, A_2 = 1.6°, D_2 = 440 mm, and R_3 = 1.2:1.0 had the highest frequencies, indicating they were the most optimal parameters for the final recommended solution.

Table 6. Frequency of each factor level.

Factor level	G_1	G_2	G_3	A_1	A_2	A_3
Frequency	1/10	3/10	6/10	1/10	8/10	1/10
Factor level	D_1	D_2	D_3	R_1	R_2	R_3
Frequency	4/10	6/10	0/10	0/10	4/10	6/10

5. Numerical analysis in flow field of optimal solution

5.1. Hydraulic performance of optimized turbine

The initial output and hydraulic efficiency of the designed turbine were 5.7 MW and 83.43%, respectively [23], which became 5.45 MW and 84.05% for the optimal turbine, respectively. **Figure 9** illustrates the hydraulic performance of the optimal turbine, where the high hydraulic efficiency region (η > 80%) is highlighted with a red circle. This high-efficiency zone, where the water head ranged between 5 m and 10 m, is suitable for tidal energy. The best hydraulic efficiency point is indicated by a red square in **Figure 9**, where η = 84.14% and H = 6.4 m.

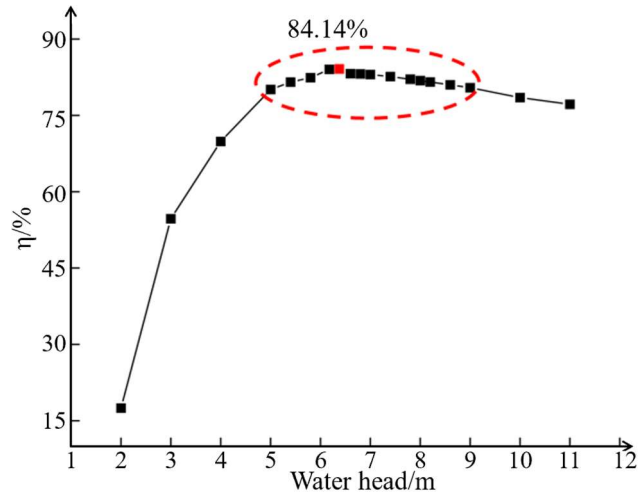

Figure 9. Hydraulic efficiency.

Figure 10(a) and **10(b)** present the velocity streamlines in the designed and optimized turbines, respectively, under the best efficiency point (BEP) condition. The velocity streamlines in the flow passage are depicted using a legend (0~20 m/s) above

the figures for velocity contours in Sections B-B and C-C (inlet and outlet of runner blades). Section A-A is the inlet of the guide vane, where the velocity of the streamlines is shown using the left legend (2.6~3.2 m/s), while the velocity of the streamlines in Section D-D, located 3 m away from the draft tube inlet, are shown using the right legend (0~6 m/s). No vortex phenomena, such as secondary flow, flow separation, or reflux, were observed in the flow domains before the draft tube in either turbine. The flow changes in each part conformed to the working principle of the turbine, wherein the fish were carried by the high-speed flow.

When **Figure 10(a)** and **10(b)** are compared, the optimized turbine showed a better distribution of the flow pattern in the guide vane with a higher velocity. Notably, the runner's hierarchical gradient of flow velocity in the draft tube (Section D-D in **Figure 10(a)**) was a direct cause of vortex rope and fluid instability, as shown in **Figure 11(a)**. This circumstance was ameliorated in the optimized turbine, as shown in **Figure 10(b)** for Section D-D.

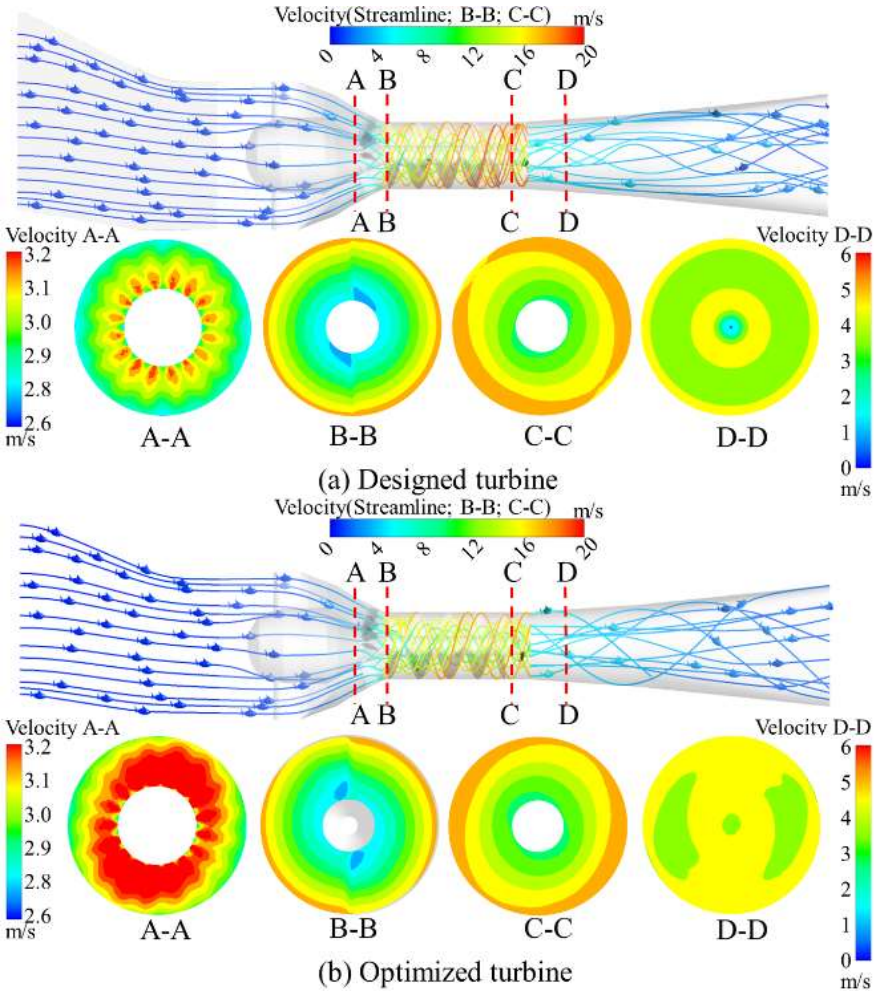

Figure 10. Flow characteristics in designed and optimized turbines.

The flow near the draft tube inlet exhibited a circumferential velocity component due to the inevitable rotation of the runner. The criterion of $Q = 0.149\ s^{-2}$ was used to identify the vortex core in **Figure 11(a)** and **11(b)**. The vortex depicted by the streamlines in the draft tube corresponded to the vortex rope, with the optimized turbine showing lower swirling strength and a smaller cortex core. The surrounding

water flowed towards the low-pressure vortex region, influenced by gravity, resulting in asymmetry along the axis compared with the vertical axis. In addition, the flow velocity decreased progressively from the inlet to the outlet of the draft tube, reflecting its strong ability for energy recovery.

Four cross-sections illustrated the velocity swirling strength in the draft tube. **Figure 11(b)** exhibits a more uniform pressure distribution in the optimized turbine. All sections showed low pressure in the central regions, where the pressure gradually increased from the center to the pipe wall, a phenomenon that weakened along the flow direction in the draft tube.

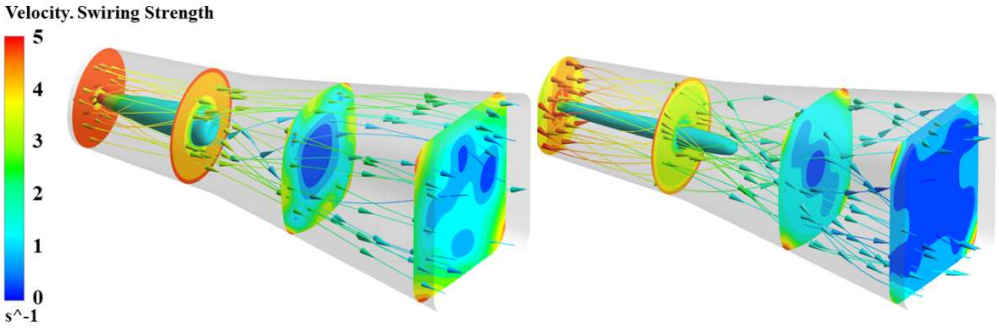

(a) The designed turbine (b) The optimized turbine

Figure 11. Flow fields in the draft tube.

5.2. Frequency characteristics of pressure in optimized turbine

A series of pressure monitoring points were set in the flow channel to explore frequency characteristics in the optimized turbine (**Figure 12**). Monitoring points IP1 to IP4 were located at the inlet pipe, where the main frequencies were two times the runner's RF (rotating frequency, at f_n = rotating speed/60 = 1.13 Hz). The main frequencies were equal to BPF (blade passage frequency, at $2f_n$ = number of runner blades × RF = 2.26 Hz), which illustrated that the pressure fluctuation in the inlet pipe was primarily influenced by runner rotation.

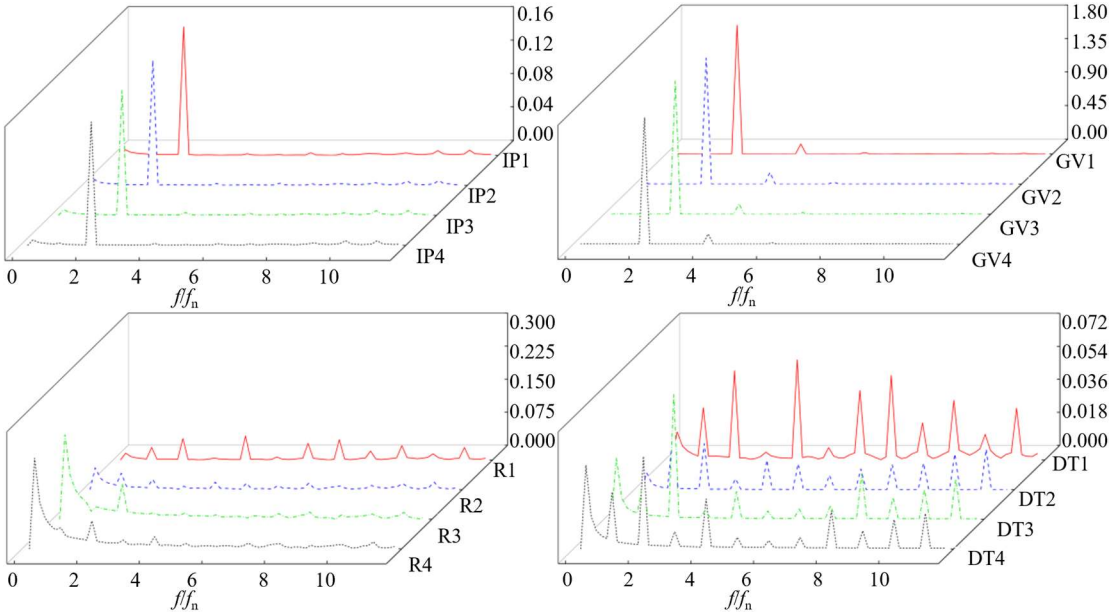

Figure 12. Frequencies of pressure in different flow domains.

Monitoring points GV1 to GV4 were positioned in the guide vane area, where the main frequencies were also $2f_n$. However, the second frequency was $4f_n$, demonstrating that runner rotation had a stronger impact on pressure fluctuations in this domain compared with that at the inlet pipe. Both IP1 to IP4 and GV1 to GV4 were evenly distributed along the circumference in their respective domains, resulting in similar amplitudes.

Monitoring points R1 to R4 were arranged along the streamlines, exhibiting various amplitudes for each frequency. Monitoring pointR1 had the highest amplitude at $4f_n$ due to its proximity to the guide vane. Monitoring points R2 to R4 had the biggest amplitudes at $0.167f_n$, with the pressure pulsation amplitude increasing along the streamline direction, which was attributable to the low-frequency pulsation caused by the vortex in the draft tube.

The frequency characteristics in the draft tube were similar to those in the runner. Monitoring points DT3 and DT4 were in the same part and had almost equal frequency amplitudes. Monitoring points DT1 and DT2 were in the same section, but DT1 had a higher amplitude at each frequency, owing to vortex influence.

5.3. Fish-passing performance analysis

The motion of the fish models being carried by the water flow in the optimized turbine was considered, while the autonomous movement of the fish models was ignored due to the high-velocity flow in the turbine. Five positions of the fish models along a single streamline were analyzed, along with each model's surface pressure, as illustrated in **Figure 13**. The surface pressure trends were similar for all fish models, where the pressure gradually decreased from tail to head. Fish1 was in a safer location in the inlet tube with relatively constant pressure. Fish2 and Fish3 were situated in the guide vane and the runner, respectively, where significant pressure energy was converted into kinetic energy. The maximum and minimum pressure differences on the surface of Fish2 and Fish3 were both about 3.6 kPa, highlighting the areas of the guide vane and the runner as critical components for the design and optimization of a fish-friendly turbine. The surface pressure on Fish5 slightly increased from tail to head due to the lower flow energy in the draft tube. The pressure on the fish models' surface throughout the entire flow passage remained above the damage threshold (50.66 kPa) [17], ensuring the safety of fish to pass through the optimized turbine.

Figure 14(a) shows five zones where pressure was lower than –15 kPa, which were Z1, Z2, Z3, and Z4, located at the inlet and outlet of the blades, as well as Z5, located around the runner cone near the outlet. In **Figure 14(b)**, Z5 disappeared, and the volume of the fish-damage area was about 0.021 m^3 (pressure < –15 kPa), which was smaller than that of the original design (the volume of the fish-damage area was about 0.03 m^3). For the optimized turbine, the shear force was less than 500 s^{-1}, indicating no shear damage to fish in the runner. The fish-passing damage rate was approximately 0.01%, calculated using $P(A) = (V_p+V_s)/V_{total}$), where V_{total} = 266 m^3.

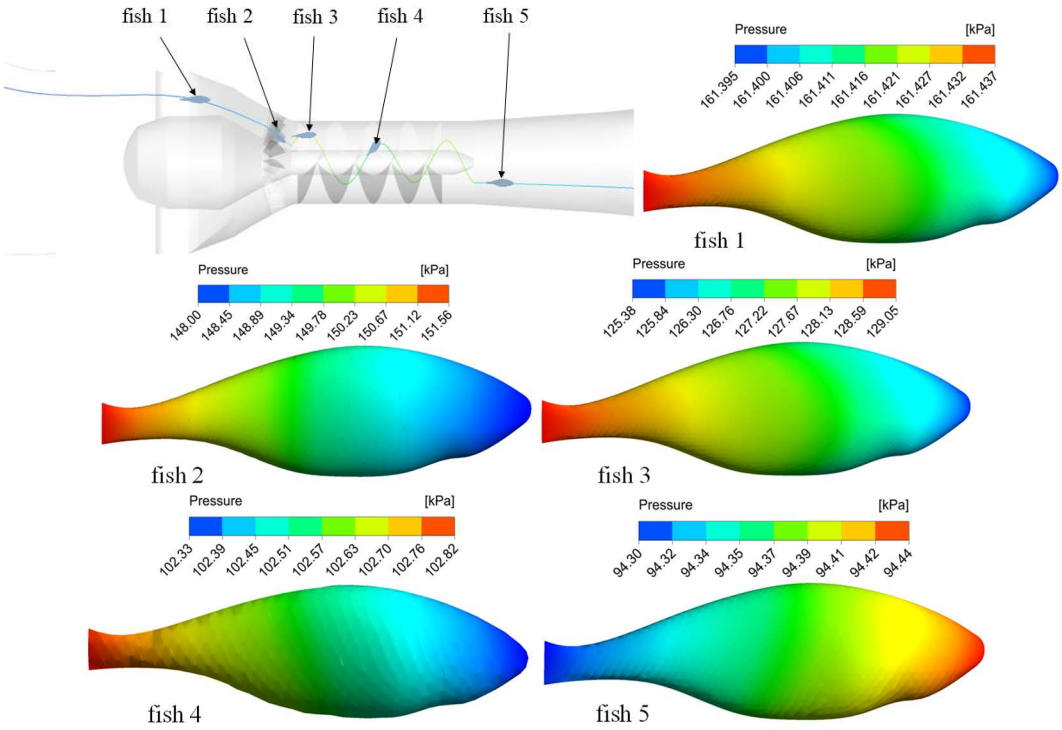

Figure 13. Fish models' positions on a single streamline, and surface pressure distributions on fish models.

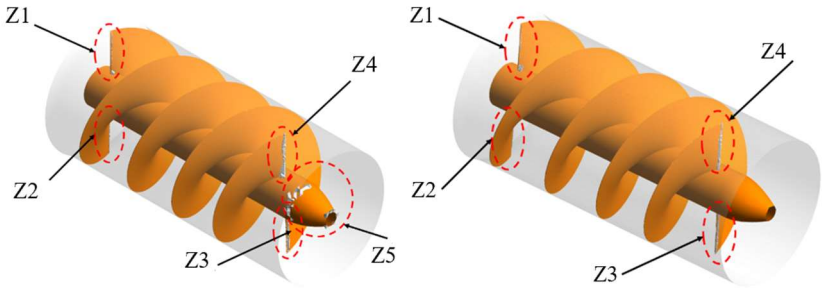

(a) The designed turbine (b)The optimized turbine

Figure 14. Pressure damage zones of fish models in runner.

6. Stress and modal analysis of runner in structural field

A runner with spiral blades has a longer axis than that of a traditional bulb turbine, making its shaft more prone to swing vibration under the same critical hydraulic excitation force. Moreover, fatigue failure is more likely to occur on spiral blades with longer shafts, potentially leading to accidents. Consequently, it is crucial to investigate the stress and natural vibration characteristics of a fish-friendly runner. The runner in this study theoretically had an infinite number of vibration modals, but in practice, only the superpositions of the first six orders of modals were considered.

6.1. Stress and modal analyses of runner

Figure 15 shows the equivalent stress distribution of the runner. The maximum equivalent stress on the blades was 74.302 MPa, mainly concentrated at the junction of the inlet edge root and the turbine shaft. In the radial direction, stress decreased from the root to the leaf edge, with the lowest equivalent stress near the leaf edge. This phenomenon occurred because the fixed constraint was set at the root of the turbine shaft. As the axial flow continued to act on the surface of the spiral blades, a large

shear force and torque were generated at the connection between the blades and the turbine shaft. In the axial direction, stress decreased from the inlet to the discharge cone along the axial direction due to the pressure energy conversion characteristics in the runner chamber. Pressure energy decreased along the flow direction, causing the pressure load on the blades' surface to gradually decrease.

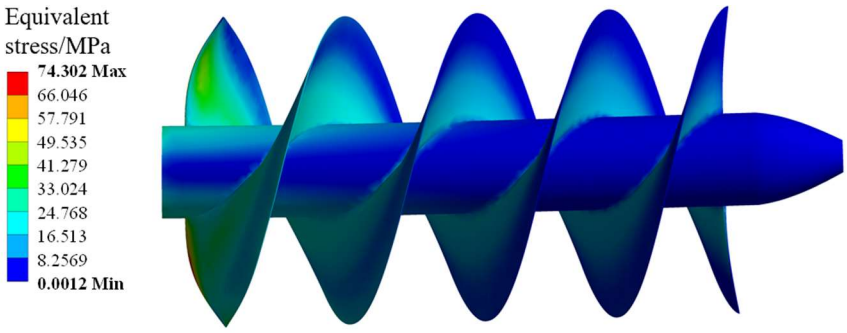

Figure 15. Stress distribution of runner.

Figure 16 exhibits the first six modes of runner vibration under a dry modal. The modal frequency of each mode increased with a larger modal order. The first and second modes, the third and fourth modes, and the fifth and sixth modes were repeated. Under these repeated modes, runner vibration showed different patterns when the runner's rotating frequency and natural frequency were the same. The vibration patterns of the first and second modes were symmetrical, resembling the swing of a pendulum, with a 90° difference in the vibration angle. Minimum deformation occurred near the shaft, with d_{max} appearing at the end of the runner cone and deformation increasing along the axial and radial directions.

The vibration patterns of the third and fourth modes manifested as the superposition of axial and radial bending. There was no obvious tensile deformation in the axial direction, whereas the deformation of the spiral blades increased along the axial and radial directions, with d_{max} appearing at the outer edge of the spiral blades near the outlet. The vibration modes of the fifth and sixth orders were dominated by the axial deformation of the spiral blades. In addition, all vibration patterns of the runner under the prestressed modal were consistent with those under the dry modal.

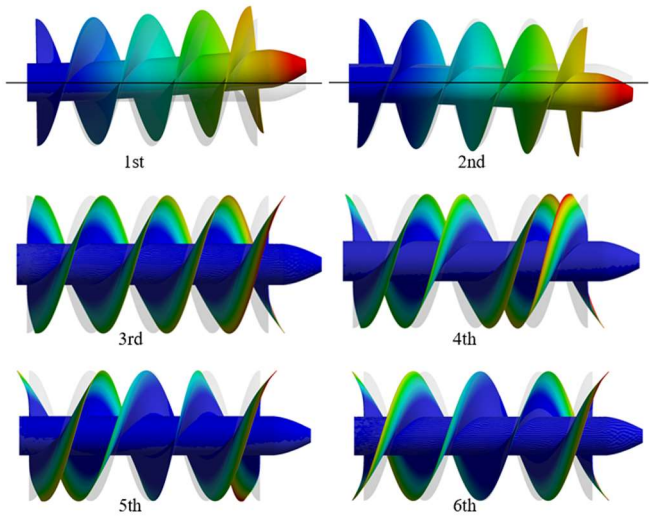

Figure 16. Vibration patterns of runner under dry modal.

Figure 17 shows the first six modes of runner vibration under the wet modal. The spiral blades bent in the axial direction in the first and second modes, with deformation increasing gradually in both axial and radial directions, and d_{max} appearing at the outer edge of the spiral blades near the outlet. In the third and fourth modes, in addition to the main axial deformation of the spiral blades, there was also circumferential torsional deformation. The vibration patterns of the fifth and sixth modes resembled the swing of a pendulum, with a 90° difference in the vibration angle, and d_{max} appearing at the outer edge of the blades.

In summary, the vibration patterns of the runner under different modals were classified into three types: swing, bending deformation, and circumferential torsion. It is noteworthy that the low-order vibration patterns with similar frequencies are symmetric due to the circumferential symmetry of the structure and constraints.

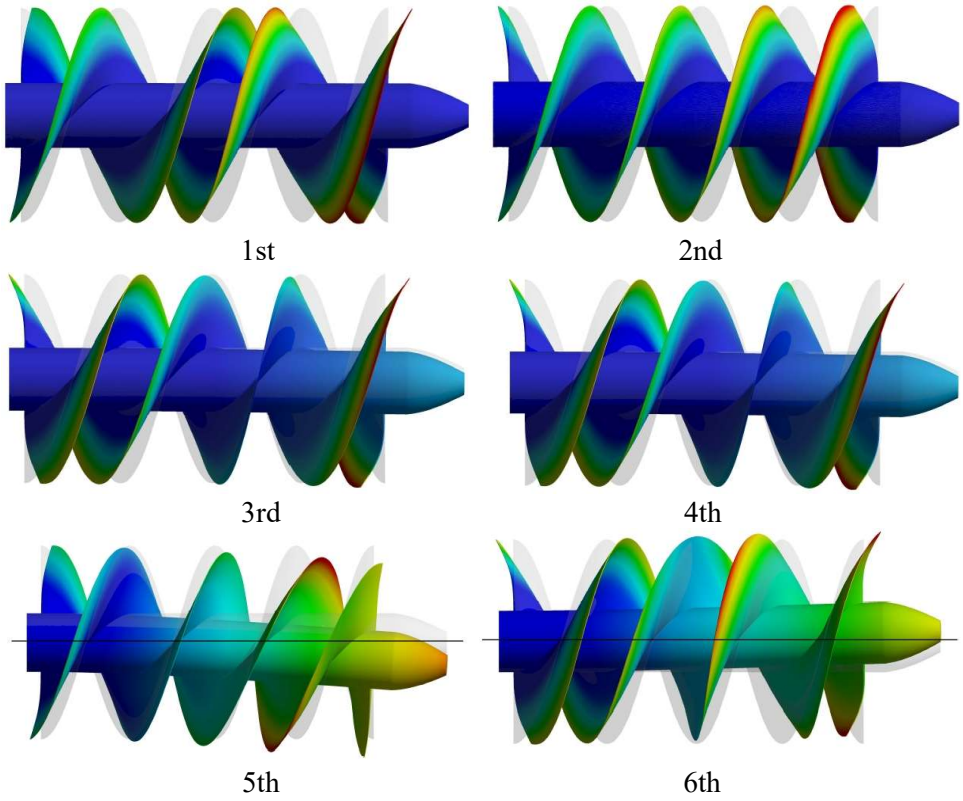

Figure 17. Vibration patterns of runner under wet modal.

6.2. Natural frequency analysis of runner under different modals

The natural frequencies of the runner for the first six orders of vibration under dry, wet, and prestressed modals are listed in **Table 7** and shown in **Figure 18**. The natural frequencies of the runner under the prestressed modal were smaller than those under the dry modal after applying water pressure, with a maximum difference of only 0.94%. This illustrates that the correlation between the runner's natural frequency and the prestressing force was weak, although the runner's stiffness improved after water pressure was loaded on the blades' surface. Compared with the prestressed modal, the natural frequencies of the runner in each order under the wet modal were reduced by approximately 39% to 61%, primarily due to the significant damping effect of water.

Table 7. Natural frequencies of runner under constrained modal.

Order	Dry modal (Hz)	Prestressed modal (Hz)	Wet modal (Hz)
1	8.55	8.47	5.12
2	8.56	8.49	5.63
3	15.54	15.51	7.21
4	15.60	15.57	7.60
5	20.35	20.3	7.72
6	20.57	20.52	7.89

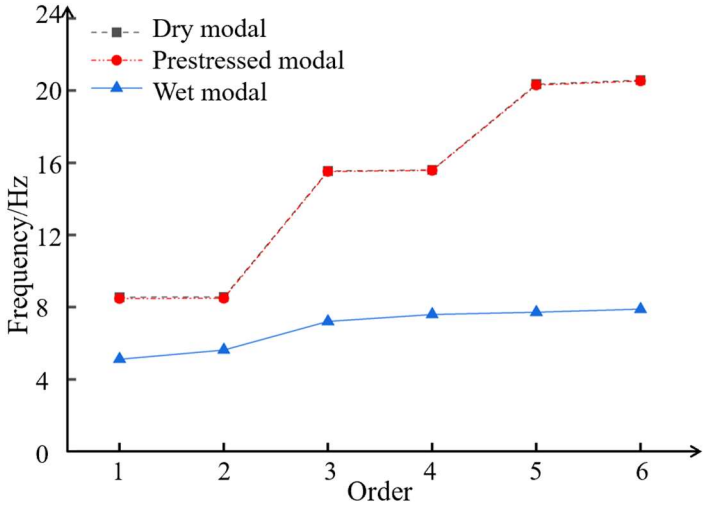

Figure 18. Natural frequencies of optimized turbine runner.

To investigate flow-induced resonance, the vortex street frequency caused by the wake flow of the guide vanes and the runner's rotating frequency was compared with the runner's natural frequency. The margins between the runner's natural frequency and various hydraulic excitation frequencies were calculated to assess the possibility of resonance. Equation (8) gives an expression of the margin (M), where f_n is the resonance frequency of the runner at the Nth order, while f is the frequency acquired from the structure's surface under the effect of the hydraulic excitation force. A margin is generally required to exceed 20% to ensure that the hydraulic excitation frequency will not induce resonance.

$$M = |(f_N - f)/f| \times 100\% \quad (8)$$

Table 8 shows that the resonance caused by hydraulic excitation did not occur in this fish-friendly turbine. Specifically, the M values were larger than 20% for the first to sixth order under the wet modal.

Table 8. Typical values of hydraulic excitation frequency, resonance frequency, and margin.

Excitation source	Computing formula	Frequency (Hz)	Margin
Rotational frequency	f	1.13	>20%
Blade passing frequency	$2f$	2.26	>20%
Guide vane passing frequency	$17f$	19.26	>20%

7. Conclusion

The optimization of the orthogonal method was conducted in this study to enhance the performance of a fish-friendly turbine by considering four control factors: the number of guide vanes (G), blade wedge angle (A), the distance of vaneless space (D), and the pitch variation ratio (R). A numerical simulation was adopted to validate the optimization work. The output, hydraulic efficiency, pressure fluctuation, blade deformation, and fish-passing damage rate of the turbine were evaluated. The SST k-ω model was used to solve the internal flow field of the turbine, while the fluid-solid coupling method was used to investigate the structural field. In this study, the effect of the internal fluid on fish within the turbine was preliminarily discussed, with fish behavior to be explored in subsequent studies. The two-bladed runner minimized the probability of fish strangulation before the inlet, compared with multi-bladed fish-friendly turbines in the literature. The main results are as follows:

(1) The optimal combination of design parameters was G = 17, A = 1.6°, D = 440 mm, and R = 1.2:1.0. Both hydraulic performance and fish-passing performance were improved in this optimized turbine, achieving 84.05% hydraulic efficiency and a 0.01% fish damage rate, respectively.

(2) The range analysis indicated that each control factor affected various indexes differently. Specifically, G significantly influenced η, $P(A)$, $d_{\max}$, and $C_{p\max}$. Parameters A and D had a greater impact on η and N, respectively, while R significantly affected $d_{\max}$ and C_{pmax}. These findings provide valuable references for similar hydraulic machinery design works.

(3) The structural field demonstrated that runner vibration patterns showed swing, bending deformation, and circumferential torsion. The runner's natural frequencies and vibration patterns were essentially the same under the dry modal and prestressed modal. However, the runner's natural frequencies under the wet modal were higher than those under the prestressed modal, with a maximum difference of 61%.

In addition to the turbine design, design optimization, and performance research in this work and our previous work [23], we will investigate cavitation and sediment erosion properties, as well as the effect of flow-induced noise on fish in future studies.

Data availability: Data will be made available on request.

Author contributions: XM: conceptualization, supervision, funding acquisition, project administration, formal analysis, investigation, methodology, writing-original draft and review. JL: data curation, formal analysis, investigation, methodology, software, writing-original draft. CC, JH, and TC: software. ZL, WH, and DC: review & editing. All authors have read and agreed to the published version of the manuscript.

Funding: This work was supported by the National Natural Science Foundation of China (51909222), China Postdoctoral Science Foundation (2024M752625), postdoctoral special funding project of Shannxi province (2023BSHTBZZ22), the second "Young Talent Promotion" held by China Society for Hydropower Engineering (CSHE-YESS-2024006), open research subject of key laboratory of fluid and power machinery (Xihua University), ministry of education (szjj2023-8). Xiuli

Mao gratefully acknowledges the financial support provided by the China Scholarship Council (No.202206305003).

Conflict of interest: The authors declare that they have no known competing financial interests or personal relationships that could have appeared to influence the work reported in this paper.

Abbreviations

R&D	Research and development	t	Pitch; m
BEP	Best efficient point	M	Torque; kN·m
SST k-ω	Shear stress transport turbulence model	ω	Angular velocity; rad/s
GGI	General graphics interface	Q	Flow rate; m^3/s
BPF	Blade passage frequency	H	Water head; m
RF	Rotating frequency	P	Pressure; Pa
Symbols		Pa	Average pressure; Pa
G	Number of guide vanes; -	V_p	Area of low-pressure damage; m^3/s
A	Blade wedge angle; °	V_s	Volume where the shear force is greater than $500s^{-1}$; m^3/s
D	Distance of vaneless space; m	V_{total}	Volumes of runner chamber; m^3/s
R	Pitch ratio; -	$d_{\max}$	Maximum blade deformation; m
α	Angle between the guide vane axis and the runner axis; °	C_{pmax}	Maximum pressure fluctuation; -
D_T	Throat diameter of guide vanes; m	C_{pmax}	Coefficient; -
i	Different levels; -	C_p	Pressure fluctuation coefficient; -
K_l	Pitch ratio; -	Y_K	Different levels of factors; -
t_r	Basic pitch; m	K_i	Sum of evaluation index values; -
N	Output; MW	$\overline{K_l}$	Average value of K_i; -
η	Hydraulic efficiency; %	R_j	Range; -
$P(A)$	Fish-passing damage rate; %	f_n	Frequency; Hz

Reference

1. Yu L, Zhou Y, Zhang F. New energy power generation technology (Chinese). China Machine Press; 2018.
2. Trabelsi M, Molina S, Charpentier JF, et al. Joint coordination of optimal power management and energy storage system sizing for a full-scale marine current turbine considering microgrid integration constraint. Journal of Energy Storage. 2022; 52: 104792. doi: 10.1016/j.est.2022.104792
3. Shetty C, Priyam A. A review on tidal energy technologies. Materials Today: Proceedings. 2022; 56: 2774-2779. doi: 10.1016/j.matpr.2021.10.020
4. Guo B, Ahmadian R, Falconer RA. Refined hydro-environmental modelling for tidal energy generation: West Somerset Lagoon case study. Renewable Energy. 2021; 179: 2104-2123. doi: 10.1016/j.renene.2021.08.034
5. Deb M, Yang Z, Haas K, et al. Hydrokinetic tidal energy resource assessment following international electrotechnical commission guidelines. Renewable Energy. 2024; 229: 120767. doi: 10.1016/j.renene.2024.120767
6. Khare V, Khare C, Nema S, et al. Tidal Energy Systems: design, optimization and control. Elsevier, 2018.
7. Damian B. Tidal Energy: The Untapped Resource. Tellwell Talent, 2023.
8. Neill SP, Haas KA, Thiébot J, et al. A review of tidal energy—Resource, feedbacks, and environmental interactions. Journal

of Renewable and Sustainable Energy. 2021; 13(6). doi: 10.1063/5.0069452
9. Khare V, Bhuiyan MA. Tidal energy-path towards sustainable energy: A technical review. Cleaner Energy Systems. 2022; 3: 100041. doi: 10.1016/j.cles.2022.100041
10. Chowdhury MS, Rahman KS, Selvanathan V, et al. Current trends and prospects of tidal energy technology. Environment, Development and Sustainability. 2020; 23(6): 8179-8194. doi: 10.1007/s10668-020-01013-4
11. Lisboa AC, Vieira TL, Guedes LSM, et al. Optimal analytic dispatch for tidal energy generation. Renewable Energy. 2017; 108: 371-379. doi: 10.1016/j.renene.2017.02.058
12. Yang C, Li Q, Xu D, et al. Fish damage due to tubular turbine: Experiments and CFD simulations. Ocean Engineering. 2023; 272: 113881. doi: 10.1016/j.oceaneng.2023.113881
13. Zhu G, Guo Y, Feng J, et al. Analysis and reduction of the pressure and shear damage probability of fish in a Francis turbine. Renewable Energy. 2022; 199: 462-473. doi: 10.1016/j.renene.2022.08.158
14. Macias MM, Mendes RCF, Garcia-Ortiz JH, et al. Numerical study of a fish swimming in hydrokinetic turbine wake. Journal of Ocean Engineering and Science. 2024. doi: 10.1016/j.joes.2024.03.001
15. Vikström L, Leonardsson K, Leander J, et al. Validation of Francis–Kaplan Turbine Blade Strike Models for Adult and Juvenile Atlantic Salmon (Salmo Salar, L.) and Anadromous Brown Trout (Salmo Trutta, L.) Passing High Head Turbines. Sustainability. 2020; 12(16): 6384. doi: 10.3390/su12166384
16. Koukouvinis P (Foivos), Anagnostopoulos J. State of the Art in Designing Fish-Friendly Turbines: Concepts and Performance Indicators. Energies. 2023; 16(6): 2661. doi: 10.3390/en16062661
17. Zhu G, Li J, Feng J. Research on Casualty Characteristics of Fish in Tubular Turbine based on IB-LBM method. Journal of Physics: Conference Series. 2020; 1549(4): 042135. doi: 10.1088/1742-6596/1549/4/042135
18. Pan Q, Shi W, Zhang D, et al. Fish-friendly design of an axial flow pump impeller based on a blade strike model. Proceedings of the Institution of Mechanical Engineers, Part A: Journal of Power and Energy. 2019; 234(2): 173-186. doi: 10.1177/0957650919849768
19. Romero-Gomez P, Colotelo A, Weissenberger S. Quantifying the Effect of Kaplan-Type Runner Blade Gaps on Fish-related Flow Conditions. IOP Conference Series: Earth and Environmental Science. 2021; 774(1): 012148. doi: 10.1088/1755-1315/774/1/012148
20. YoosefDoost A, Lubitz W. Archimedes Screw Turbines: A Sustainable Development Solution for Green and Renewable Energy Generation—A Review of Potential and Design Procedures. Sustainability. 2020; 12(18): 7352. doi: 10.3390/su12187352
21. Lyons M. Lab testing and modeling of Archimedes screw turbines [PhD thesis]. The University of Guelph; 2014.
22. Zhang P, Hu D, Cheng Y, et al. Fish-friendly turbine with two counter-rotating runners. Concepts and runner optimization. Journal of Hydroelectric Engineering, 2021; 40(8): 65-72. doi: 10.11660/slfdxb.20210807
23. Lu J, Mao X, Wang Y, et al. Development and numerical test of fish-friendly turbine for tidal energy. Proceedings of the CSEE. 2023; 43(16): 6340-6348. doi: 10.13334/j.0258-8013.pcsee.221024
24. Fu T, Deng ZD, Duncan JP, et al. Assessing hydraulic conditions through Francis turbines using an autonomous sensor device. Renewable Energy. 2016; 99: 1244-1252. doi: 10.1016/j.renene.2016.08.029
25. Mueller M, Knott J, Pander J, et al. Experimental comparison of fish mortality and injuries at innovative and conventional small hydropower plants. Journal of Applied Ecology. 2022; 59(9): 2360-2372. doi: 10.1111/1365-2664.14236
26. Brown RS, Carlson TJ, Gingerich AJ, et al. Quantifying Mortal Injury of Juvenile Chinook Salmon Exposed to Simulated Hydro-Turbine Passage. Transactions of the American Fisheries Society. 2012; 141(1): 147-157. doi: 10.1080/00028487.2011.650274
27. Huang Z, Cheng Y, Wu J, et al. FSI simulation of dynamics of fish passing through a tubular turbine based on the immersed boundary-lattice Boltzmann coupling scheme. Journal of Hydrodynamics. 2022; 34(1): 135-147. doi: 10.1007/s42241-022-0014-7
28. Yang C, Xu D, Zhu S, et al. Analysis and research on fish damage caused by internal pressure change of tubular turbine. Journal of Hydraulic Engineering. 2021; 52(6):731-738. doi: 10.13243/j.cnki.slxb.20200691
29. Zhu L, Zhang F, Shi X, et al. A Systematic Investigation on the Damage Characteristics of Fish in Axial Flow Pumps. Processes. 2022; 10(11): 2228. doi: 10.3390/pr10112228
30. Koukouvinis P (Foivos), Anagnostopoulos J. Simulating Fish Motion through a Diagonal Reversible Turbine. Energies. 2023; 16(2): 810. doi: 10.3390/en16020810
31. Richmond MC, Romero-Gomez P, Serkowski JA, et al. Comparative Study of Barotrauma Risk during Fish Passage through

Kaplan Turbines. Office of Scientific and Technical Information (OSTI); 2015. doi: 10.2172/1326154
32. Mueller M, Sternecker K, Milz S, et al. Assessing turbine passage effects on internal fish injury and delayed mortality using X-ray imaging. PeerJ. 2020; 8: e9977. doi: 10.7717/peerj.9977
33. Baumgartner LJ, Thorncraft G, Phonekhampheng O, et al. High fluid shear strain causes injury in silver shark: Preliminary implications for Mekong hydropower turbine design. Fisheries Management and Ecology. 2017; 24(3): 193-198. doi: 10.1111/fme.12213
34. Zhou J, Zhao M, Wang C, et al. Optimal Design of Diversion Piers of Lateral Intake Pumping Station Based on Orthogonal Test. Zhu Y, ed. Shock and Vibration. 2021; 2021(1). doi: 10.1155/2021/6616456
35. Xu Y, Tan L, Cao S, et al. Multiparameter and multiobjective optimization design of centrifugal pump based on orthogonal method. Proceedings of the Institution of Mechanical Engineers, Part C: Journal of Mechanical Engineering Science. 2016; 231(14): 2569-2579. doi: 10.1177/0954406216640303
36. Mao X, Liu Z, Li T, et al. A brief review of numerical solving methods for internal fluid of pumped storage unit. International Journal of Energy Research. 2020; 44(10): 7886-7902. doi: 10.1002/er.5474
37. Gu J, Cai F, Müller N, et al. Two-Way Fluid–Solid Interaction Analysis for a Horizontal Axis Marine Current Turbine with LES. Water. 2019; 12(1): 98. doi: 10.3390/w12010098
38. Xin L, Li Q, Li Z, et al. Analysis of Runner Dynamics of Reversible Hydraulic Turbine by Alternating Fluid–Solid Action. Frontiers in Energy Research. 2022; 10. doi: 10.3389/fenrg.2022.943339
39. Sun J, Zhou Y, Ge X, et al. Research on Multiobjective Optimization of Bulb Tubular Turbine Based on Orthogonal Test. Zhou L, ed. Shock and Vibration. 2021; 2021(1). doi: 10.1155/2021/5581455
40. Chen J, Zheng Y, Zhang L, et al. Optimization of geometric parameters of hydraulic turbine runner in turbine mode based on the orthogonal test method and CFD. Energy Reports. 2022; 8: 14476-14487. doi: 10.1016/j.egyr.2022.10.444
41. Southern Illinois University. Chapter 8 Orthogonal Designs. Available online: http://parker.ad.siu.edu/Olive/rch8.pdf (accessed on 12 August 2024).
42. Zuo Z, Liu S, Sun Y, et al. Pressure fluctuations in the vaneless space of High-head pump-turbines—A review. Renewable and Sustainable Energy Reviews. 2015; 41: 965-974. doi: 10.1016/j.rser.2014.09.011
43. Ke C, Xiong L, Peng N, et al. Numerical and experimental study of the performance effects of varying vaneless space in high-speed micro turbine stators. Cryogenics. 2017; 88: 10-16. doi: 10.1016/j.cryogenics.2017.09.004
44. Rode BR, Kumar A. Unstable pressure fluctuations in the vaneless space of high-head reversible pump-turbines – A systematic review. Journal of Energy Storage. 2023; 72: 108397. doi: 10.1016/j.est.2023.108397